npj | 2D materials and applications

www.nature.com/npj2dmaterials

ARTICLE OPEN

Laser-assisted explosive synthesis and transfer of turbostratic graphene-related materials for energy conversion applications

Kapil Bhorkar[1,2,5], Nikolaos Samartzis[1,3,5], Michail Athanasiou[1], Labrini Sygellou[1], Nikos Boukos[4], Vassilios Dracopoulos[1], Theophilos Ioannides[1] and Spyros N. Yannopoulos[1]✉

Production of high-grade graphene-like materials using a simple, reliable processes and its simultaneous transfer onto soft surfaces have not yet achieved; hence impeding wide-ranging graphene applications. Even more complex processes are required to prepare graphene-based nanohybrids, which offer additional synergistic functionalities in relation to graphene. Here, an uncomplicated and scalable process to prepare high-purity few-layer turbostratic graphene and graphene/SiO_x nanohybrids is demonstrated employing laser-mediated explosive synthesis and transfer of graphene flakes. The process is capable of producing, and simultaneously transferring, graphene flakes on any substrate, such as polymer, glass, metal, ceramics, etc. Graphene and nanohybrids exhibit sp^2 structures of turbostratic stacking, with low sheet resistance and very high (~30) C/O ratio. The merits of the method are showcased by two energy-related examples, flexible single-electrode triboelectric nanogenerators and electric double-layer capacitors. This method emerges as a paradigm of additive manufacturing for graphene-based devices with impact for applications in flexible electronics.

npj 2D Materials and Applications (2022)6:56 ; https://doi.org/10.1038/s41699-022-00331-7

INTRODUCTION

Graphene and graphene-related materials (GRMs) have profoundly dominated in science and technology over one and a half decade[1,2]. These materials have attracted particular attention owing to the supreme properties of monolayer graphene, which raised great expectations for a number of applications. Indeed, GRMs have been explored for a wide range of applications, including primarily microelectronics[3], and other sectors as well, ranging from sensors, membranes, flexible electronics, energy conversion/storage devices, various functional coatings, up to concrete additives[4]. However, in their vast majority, real-world viable applications of graphene have remained rather unachieved or at least have not reached the level foreseen a decade ago[5]. The main cause has been the inadequacy of the current synthesis methods to scale up production of graphene with appropriate quality. The trade-off between quality and scalability has evolved towards the development of graphene-like structures or GRMs suitable for less-demanding applications placing the emphasis on particles, platelets, and 3D graphene structures, such as foams and porous networks. Selected commercial products, e.g., sports goods, inks, and coatings, are currently using GRMs as additives[6]. However, current industrial production has not yet managed to bear up with the specified quality of GRMs suitable to particular needs. GRMs are produced today with varying properties spanning a range of quality from graphene-like to graphite-like. As a result, the production of GRMs at large volume with consistent quality is still elusive, stemming progress in their integration into devices. Indeed, a recent scrutiny concerning "commercial graphene" powders produced by more than sixty companies worldwide, concluded that these powders predominantly consist of graphite particles[7]. This study advocates that the poor quality of the commercial "graphene" is the main source of the long delay of pertinent applications.

Laser-based methods for graphene and GRMs synthesis have much less been employed over the first decade of the graphene era, in comparison to classical wet-chemistry and high-temperature vacuum chamber methods. The sporadic attempts appearing initially have gained ground over the last years in view of the versatility offered by the use of lasers and their success in a wide variety of processes including epitaxial growth on SiC wafers[8], and SiC particles[9], decomposition of polymers[10,11] and biomass[12,13], reduction of graphene oxide[14,15], transformation of carbon materials from sp^3 to sp^2 networks[16], and related cases[17]. These recent advances testify that laser-assisted synthesis of GRMs can confront the volume/quality trade-off without compromising on lower quality, and have thus grown awareness on their optimization. In addition, the benefits of direct synthesis on any substrate, and the feasibility of in situ patterning together with the avoidance of using toxic chemicals, high-temperature, vacuum chambers, and other strict conditions, render laser-assisted methodologies compatible with current industrial processes and, hence, an emerging rival of other physical/chemical methods.

Graphene-based nanohybrids, typically GRMs decorated with other types of nanoparticles, have been explored as they can offer additional functionalities brought about by the combination and synergies of the properties of the individual components. Synthesis approaches of GRM nanohybrids typically entail various chemical methods such as hydrothermal, sol-gel, layer-by-layer, and so on, where in most cases the two components are prepared separately before being blended. These approaches require complex and time-consuming steps followed by elaborate post-treatment procedures, which unavoidably contaminate the purified material with residues affecting performance and

---

[1]Foundation for Research and Technology Hellas – Institute of Chemical Engineering Sciences (FORTH/ICE-HT), P.O. Box 1414, GR-26504 Rio-Patras, Greece. [2]Univ Rennes, CNRS, ISCR - UMR 6226, F-35000 Rennes, France. [3]Department of Physics, University of Patras, GR-26504 Rio-Patras, Greece. [4]Institute of Nanoscience and Nanotechnology (INN), National Centre for Scientific Research "Demokritos", GR-15341 Agia Paraskevi Attikis, Greece. [5]These authors contributed equally: Kapil Bhorkar, Nikolaos Samartzis. ✉email: sny@iceht.forth.gr

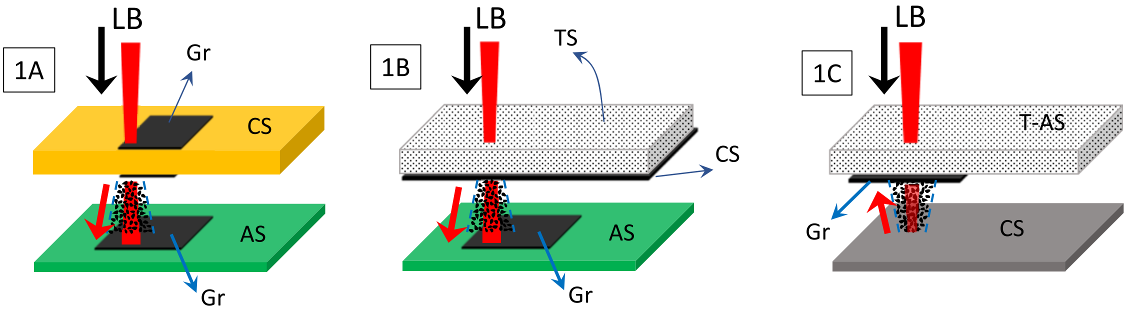

Fig. 1 Irradiation geometries. Variants of forward and backward LEST graphene synthesis and deposition onto a substrate.

durability of the device application. Representative examples of nanohybrids based on graphene and silica, include chemically reduced GO and Stöber-prepared SiO_2 nanoparticles to prepare rGO/SiO_2 for photocatalytic applications[18], rGO/SiO_2 solid films (prepared by spin-coating dispersion of GO containing silica precursors followed by chemical reduction and calcination to produce rGO and SiO_2, respectively) as transparent conductors[19], and gas sensors[20]. GRM/SiO_x hybrids have also shown promising potential in micro-wave absorption and electromagnetic shielding, in view of the synergistic effects of dielectric and magnetic loss brought about by hybridization[21]. Overall, nanohybrids based on GRMs and various nanoparticles have been prepared employing a wide variety of ways including chemical and physical methods. Currently, no attempt has been reported about the solvent-free, single-step growth and transfer of GRMs/nanoparticles hybrids by laser-assisted methods at ambient conditions.

In this article, we propose a versatile laser-based method toward the single-step, scalable production of graphene flakes and graphene-nanohybrids, at ambient conditions, avoiding any wet-chemistry pre-treatment or post-processing. The method entails the irradiation of various carbon sources (CS), i.e., polymers, and biomass-related matter, in the absence of protective environment. The irradiation takes place in an arrangement capable of simultaneously synthesizing and transferring the violently decomposed product onto any arbitrary substrate. The proposed approach, is based upon the laser-mediated explosive synthesis and transfer (LEST) of graphene flakes towards the substrate. The explosive character of the decomposition of the target compound is vital in this process, because the produced gasses impose a propelling stream, essential for the graphene flakes and graphene/nanohybrids transfer.

Various forward and backward configurations of the LEST graphene process is illustrated in Fig. 1. Figure 1A illustrates an example of a forward LEST process. The target source is a semi-transparent film (in regard to the incident laser wavelength) comprising the CS material. GRMs are deposited at the acceptor substrate (AS). Figure 1B illustrates an example where a CS layer has been pre-deposited on the rear side of a transparent substrate (TS). Graphene is deposited at the acceptor substrate (AS). Figure 1C illustrates an example of a backward LEST process where the laser beam passes unhampered through the TS and reaches the CS film. Graphene flakes are collected at the side of the TS facing the CS, while the TS plays also the role of the AS.

By applying LEST on a polyimide (PI) foil and a PI tape (PI foil covered on one side by a silicone adhesive) we show that apart from neat graphene flakes (PI irradiation) two different materials can be simultaneously decomposed (PI/silicone adhesive) providing a hybrid nanomaterial, i.e. graphene/SiO_x. The method developed in this work differs from the established laser-induced forward transfer (LIFT) from solid donor films that may include phase change during transfer of materials, such as Si and Ge[22]. The main difference is that in the current process, a polymer or an organic compound decomposes to elemental carbon; hence undergoing not simply a phase change but composition changes, at the same time. LIFT has recently been employed by Smits et al.[23] to transfer graphene which was grown by CVD and transferred onto glass substrates; the process necessitates the use of a triazene-based layer, having the role of the dynamic release layer. Additional attempts have been developed along this direction. In particular, transfer of CVD graphene has been reported using blister-based laser-induced forward transfer, exploiting the laser radiation absorption of the metallic substrate[24]. Other reports include the backward transfer of mono-layer CVD graphene from a Ni substrate to fused silica using femtosecond laser irradiation[25] and the selective forward transfer of CVD graphene with high resolution on silica and polymer-based substrates[26].

Notably, no attempt has been undertaken to achieve simultaneously the formation and transfer of GRMs and in particular graphene-based nanohybrids, by a single-step laser approach. Here, we demonstrate the feasibility of such a process, operating at ambient conditions process, by transferring graphene and graphene/SiO_x nanohybrids on any substrate. The high-purity and benefit of the obtained products is showcased by two application examples. In particular, these materials have been utilized as electrodes in devices, such as (a) flexible triboelectric nanogenerators (TENGs) scavenging and converting mechanical energy to electrical, and (b) electric double-layer capacitors (EDLCs).

RESULTS AND DISCUSSION

Structure, morphology, and composition of LEST graphene

Two types of commercial Kapton^{TM} materials were utilized as precursors for laser-assisted decomposition; a neat Kapton foil and a Kapton tape, i.e. a PI foil with one of its sides covered by a silicone adhesive film. Henceforth, the prepared and characterized samples will be referred to as LEST−*x*−*y*, with "*x*" denoting the type of precursor (F for neat Kapton foil, and T for Kapton/silicone adhesive tape) and "*y*" representing the irradiation fluence value in J cm^{-2}. It is worth-noting that a single lase at ambient atmosphere, using mm-scale spot, is sufficient to convert both the foil and tape into graphene flakes and graphene/SiO_x nanohybrids, respectively, which renders the process simple and efficient. To demonstrate the versatility of the proposed approach, the LEST process was employed to develop films on a diverse set of substrates including soft materials, glass, ceramics, metals, and so on. Typical substrates used in the current study are polydimethylsiloxane (PDMS), polyethylene terephthalate (PET), molybdenum foil, carbon fiber paper, silicon, and glass. Representative optical images are shown in Supplementary Fig. 1.

The microstructure details of these films were recorded by field-emission scanning electron microscopy (FE-SEM). Representative examples of the foam-like graphene and graphene/SiO_x nanohybrids deposited on PDMS and carbon fiber paper are illustrated in Fig. 2. The images demonstrate a highly porous structure, which originates from the violent decomposition of the

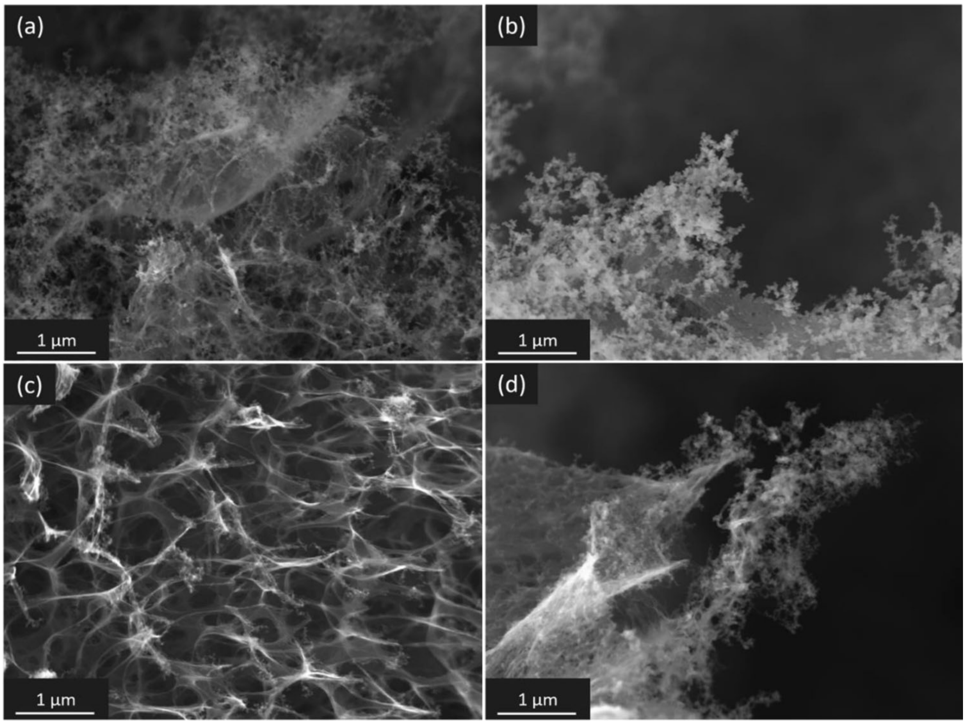

Fig. 2 Morphology via scanning electron microscopy. FE-SEM images of **a** graphene flakes and **b** graphene/SiO$_x$ nanohybrids deposited on PDMS. FE-SEM images of **c** graphene flakes and **d** graphene/SiO$_x$ nanohybrids, deposited on carbon fiber paper.

PI structure causing a rapid outgassing of oxygen and nitrogen species. In the case of PI/silicone decomposition, the graphene-like structures appear decorated with SiO$_x$ nanoparticles, Fig. 2b, d. The latter arise from the disintegration of the silicone-based adhesive layer of the Kapton tape. The thickness of the deposited graphene-based films was estimated by SEM images; see Supplementary Fig. 2a, b taken at the cross section of films deposited by LEST on glass substrates. The images show that the thickness of the films is within the range 20–30 µm but can vary depending on the laser fluence.

A more detailed view of the morphology at the nanoscale is provided by the high-resolution transmission electron microscopy (HR-TEM) images depicted in Fig. 3. Images 3a and 3b demonstrate the formation of carbon layers, showing nearly free, graphene layers at the edges of the structures. A deeper inspection reveals that few-layer stripes, comprised of 2–4 layers, percolate through the structure of the material. These observations point towards the formation of non-compact graphitic structures lending support to the few-layer graphene character of the material. The average interlayer d_{002} spacing, obtained by analyzing those images using local area fast Fourier transforms, reveals d_{002} values in the range 0.341–0.364 nm; a typical paradigm is shown in Supplementary Fig. 2c. SAED analysis shows that the interlayer spacing is far larger than that of the Bernal stacking (0.334 nm), signifying a turbostratic nature of the graphene-like structures. A large density of SiO$_x$ nanoparticles are formed when the PI/silicone adhesive material is irradiated, as shown in Fig. 3c. The size of the vast majority of these nanoparticles lies in the range 15–20 nm, while few larger ones, yet <50 nm in diameter, are also evident. Figure 3d shows a magnification of the upper right part of Fig. 3c marked in the rectangle. This image demonstrates that graphene layers are disposed wraparound the nanoparticles forming an interacting phase of the nanohybrid system. The graphene-like phase of the nanohybrid, does not present structural differences in comparison to the films obtained by the Kapton foil (neat PI) irradiation. Additional support for the turbostratic nature of the few-layer graphene flakes is provided by X-ray diffraction analysis, Supplementary Fig. 3.

The thermogravimetric analysis (TGA) of both precursors is illustrated in Supplementary Fig. 4a. Kapton is known to exhibit superior thermal stability among most polymers. TGA reveals that thermal degradation commences at ~510 °C and the degradation rate is maximized at 590 °C. The residual remaining after high-temperature heating (800 °C) amount to ~57.5% of the initial mass. The PI/silicone adhesive precursor shows mass loss starting at ~230 °C, which designates the decomposition of the silicone adhesive material. The remaining mass in this case is of ~47%. The Raman spectrum of the heat-induced carbonized products, Supplementary Fig. 4b, demonstrates the formation of nanocrystalline or amorphous carbon.

Graphitization of polyimide (Kapton) using laser beams towards formation of conductive paths on its surface has been known for long[27,28]. Detailed studies were undertaken to explore the composition of the ablated plume. Mass spectroscopy has revealed the presence of species such as C_2H_2, HCN, CO, CO_2, C_4H_2, and C_6H_2[29]. The composition of the plume depends upon the ablation fluence[30] and the chamber environment[31]. Particular attention was also paid on the deposited product following ablation[32]. Polyimide has recently been reconsidered as one of the most successfully graphitized commercial polymers[10]. Representative Raman spectra of graphene grown on the front and back side (in regard to the incidence of the laser beam) of neat PI foil are shown in Fig. 4a. The Raman spectra of LEST graphene are presented in Fig. 4b. In all these cases the spectra reveal successful transformation of the polyimide structure to sp^2 carbon networks. The comparison of the Raman spectra of graphene grown on the surface of the PI film and the spectra of LEST graphene, provides evidence that the quality of these two graphene products is similar. This observation essentially reveals that the laser-mediated transfer process of graphene does not affect its quality.

It is instructive to reminisce few important, frequently overlooked, early data related to Kapton laser-induced ablation. Preceding studies have mainly focused on the use of UV laser

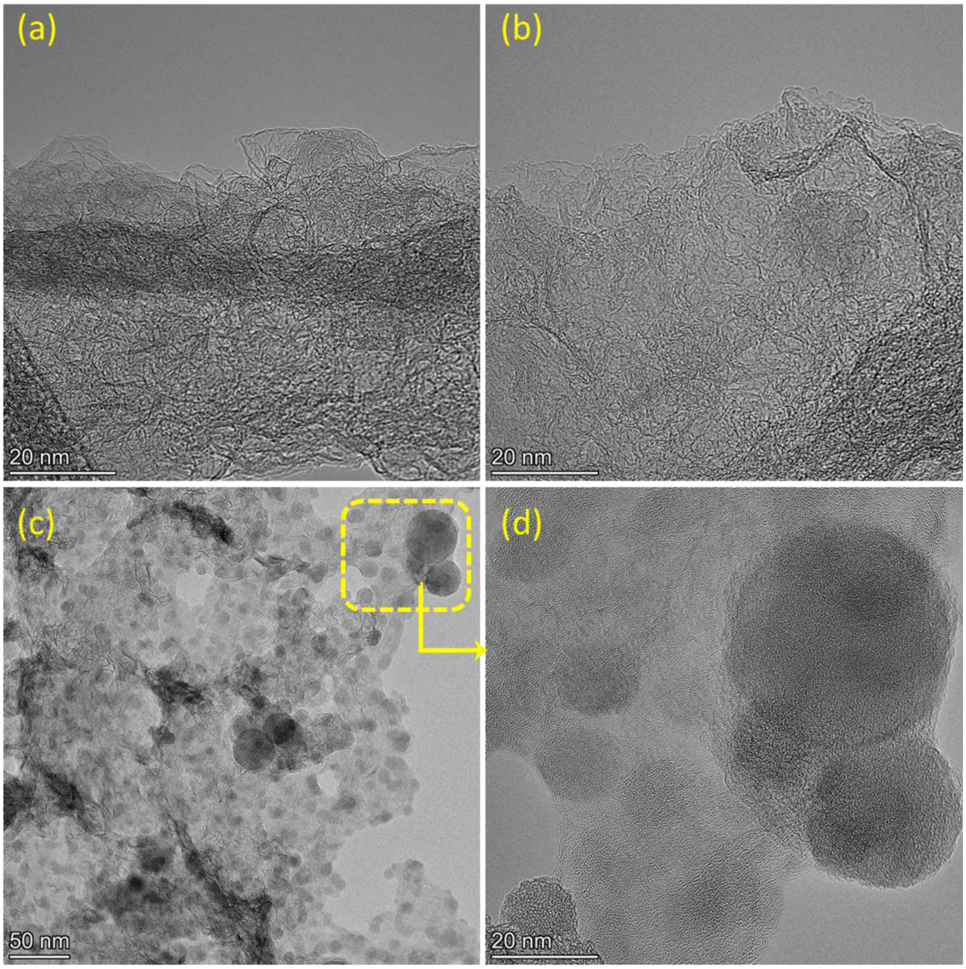

Fig. 3 Structure via transmission electron microscopy. **a**, **b** High-resolution TEM images of graphene-like structures obtained after Kapton foil PI decomposition. **c** Low magnification, and **d** HR-TEM images of graphene/SiO_x nanohybrids arising from Kapton tape (PI/silicone adhesive) laser-assisted decomposition.

ablation of polyimide films. The ablated product collected from the surface around the irradiated area was predominantly identified as carbon, in the pre-graphene era[33]. Notably, this solid product has been found to be charged, with an almost equal distribution of positively and negatively charged particles[34]. The electrostatic nature of the ablated products was assigned to the presence of ambient atmosphere[34]; indeed previous studies had shown that carbon molecular species of Kapton under irradiation are neutral[35]. Whereas these experimental facts have emerged from Kapton ablation processes related to UV irradiation (mostly 193 and 308 nm), they could handily serve to account for current observations of Kapton decomposition by a near-IR laser. In particular, the electrostatic attraction of the oppositely charged species in the gaseous phase might be a decisive factor for the enhanced adhesion and integrity of the graphene films on the surface of a wide variety of substrates, as discussed above.

The ablation mechanism of PI has been the subject of previous investigations[36] using a 20-kHz nanosecond pulsed laser operating at 1064 nm. Despite that PI exhibits very weak absorption at 1064 nm, as evidenced by the low absorption coefficient $\alpha \sim 16\ \text{cm}^{-1}$, the ablation of PI with this photon energy is still feasible. Dyer et al.[36] showed that the ablation of PI, takes place at moderate fluence in the range 3–30 J cm^{-2}. The process becomes activated after some degree of incubated absorption. Such incubation effects are potentially associated with carbonization induced by photochemical and/or thermally induced degradation. These effects can cause rise of the absorption coefficient from $\alpha \sim 16\ \text{cm}^{-1}$ to $\sim 150\ \text{cm}^{-1}$ after 15 pulses of irradiation, of ~2 ns width, which take place in <0.2 ms. In the current work, we employ the same photon energy at fluences similar to those used by the previous study[36]; however, the carbonization of PI takes place by a single pulse. The reason is that the pulse duration, 1.5 ms, is much longer than that used in the previous study. In the current case, the incubation time is certainly shorter than the pulse duration. Therefore, the incubation step for the formation of absorbing elements in the PI structure, takes place within the first fraction of the pulse duration, while the rest part of pulse energy results in fast temperature rise, graphitization, and ablation of the graphene flakes towards the acceptor substrate.

The Raman spectra show that all three main bands, D, G, and 2D are well resolvable and fairly narrow, indicating a high extent of graphitization and a rather moderate defect concentration. Typical spectral parameters resulting from Lorentzian type fitting are presented in Fig. 4b, c. In particular, the absence of skewness in the spectral shape of the 2D band is indicative of non-Bernal stacking. Bernal stacking in few-layer graphene platelets can severely diminish their electronic transport in relation to monolayer graphene, leading to properties similar to bulk graphite[37]. A series of Raman spectra obtained from the films produced by the decomposition of both precursors (Kapton foil and tape) using various laser fluences are shown in Supplementary Fig. 5 along with the analysis details. In all cases, the 2D line is evident in the spectra; whereas the optimization of graphene quality was undertaken considering the sp^2 content (D/G intensity ratio) and

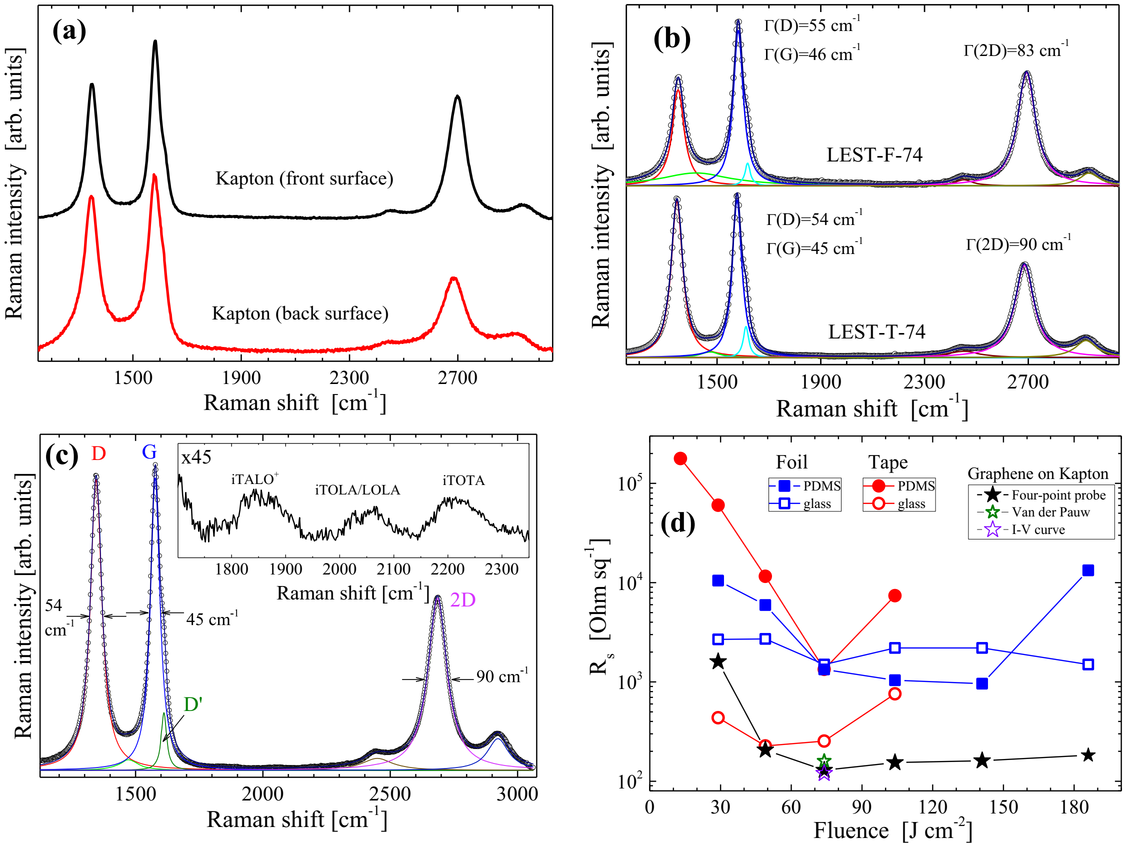

Fig. 4 Raman data and electrical properties. Raman spectra of **a** graphene flakes grown on front and back side of Kapton foil in the course of a single irradiation step, and **b** graphene flakes grown by LEST for the foil and tape precursors (fluence: 74 J cm^{-2}). **c** Lorentzian line fitting of a Raman spectrum; the inset shows in magnification the spectral area of the turbostratic peaks. **d** Sheet resistance of graphene and graphene/SiO$_x$ transferred onto glass and PDMS substrates. For comparison R$_s$ for graphene grown on Kapton foil is also presented.

the intensity of the 2D band. The spectral changes are not dramatic against laser fluence; however, the data show a fairly optimized process for LEST-74 for both the tape and the foil. The symmetric shape and single-Lorentzian character of the 2D band shown in Fig. 4a, b is characteristic of turbostratic graphene[38], lending support to the expanded d$_{002}$ interlayer spacing observed by HR-TEM. Additional evidence of the turbostratic nature of the graphene-like structures produced by laser-assisted decomposition of Kapton is provided in Fig. 4c. The turbostratic arrangement originates from rotationally faulted layers and/or layers with expanded interlayer distance. A number of weak Raman bands appear in the energy range between the G and 2D peaks. These are combination Raman bands, which can provide information about the stacking order of adjacent graphene layers[39,40], and their emergence demonstrates the formation of turbostratic arrangement of the graphene layers. In particular, the band located at ~1850 and ~2050 cm^{-1} have been associated with the iTALO and iTOLA/LOLA modes, respectively. T, L, O, and A stand for transverse, longitudinal, optic, and acoustic modes, respectively. Typically, the current findings demonstrate one of the very rare cases—a few examples being epitaxial graphene on SiC[8], biomass-produced graphene[13], and lastly polymer (phenol-based resin) derived graphene[11]—where laser-assisted decomposition of a precursor can lead to turbostratic graphene. Based on the evidence provided by three techniques, HRTEM, Raman scattering, and XRD, we conclude that the deposited films, for both cases of precursor materials, are composed of a 3D porous network of few-layer turbostratic graphene flakes. Therefore, the term graphene mentioned throughout the text should be conceived as few-layer turbostratic graphene.

The enhanced sp^2/sp^3 ratio obtained for the fluence of 74 J cm^{-2} is in accordance with the lowest sheet resistance, R_s, as shown in Fig. 4d. The figure displays the sheet resistance values of the graphene-like films prepared by Kapton foil and tape on two different substrates, i.e., glass and PDMS. The fluence dependence of R_s for graphene grown on the Kapton surface is also shown for comparison. The curve shows an appreciable decrease of R_s, while increasing fluence, reaching the value of 129 Ω sq^{-1} at 74 J cm^{-2}, followed by a mildly increasing trend for higher fluences. Either sharper or less pronounced, the curves exhibit minima in the sheet resistance dependence against fluence. It should, however, be noticed that the measured values represent an upper limit of the true R_s values of the graphene materials under investigations. It is well-perceived that the sheet resistance of a particulate system (e.g., powder or film) can be appreciably higher than that of the individual particles. The enhanced resistance arises from the gaps and interfaces between the particles which impedes carrier transport. To overcome this issue, powdered samples are pressurized to decrease interparticle gaps and increase the contact area[41]. R_s values shown here have been measured in as-prepared LEST films without any further treatment. Graphene/SiO$_x$ on glass shows the lowest R_s values, almost an order of magnitude, among the other cases shown in Fig. 4d, despite that this film consists of a large fraction of non-conducting SiO$_x$ nanoparticles. This finding could be attributed to the enhanced integrity of the film containing such oxide nanoparticles, which act as “binding” elements among graphene-like layers bridging gaps for carrier transport. The wrapping of graphene layers over the SiO$_x$ nanoparticles’ surface observed by HR-TEM, may enhance conductive pathways, hence providing a rationale for the various sets of R_s data.

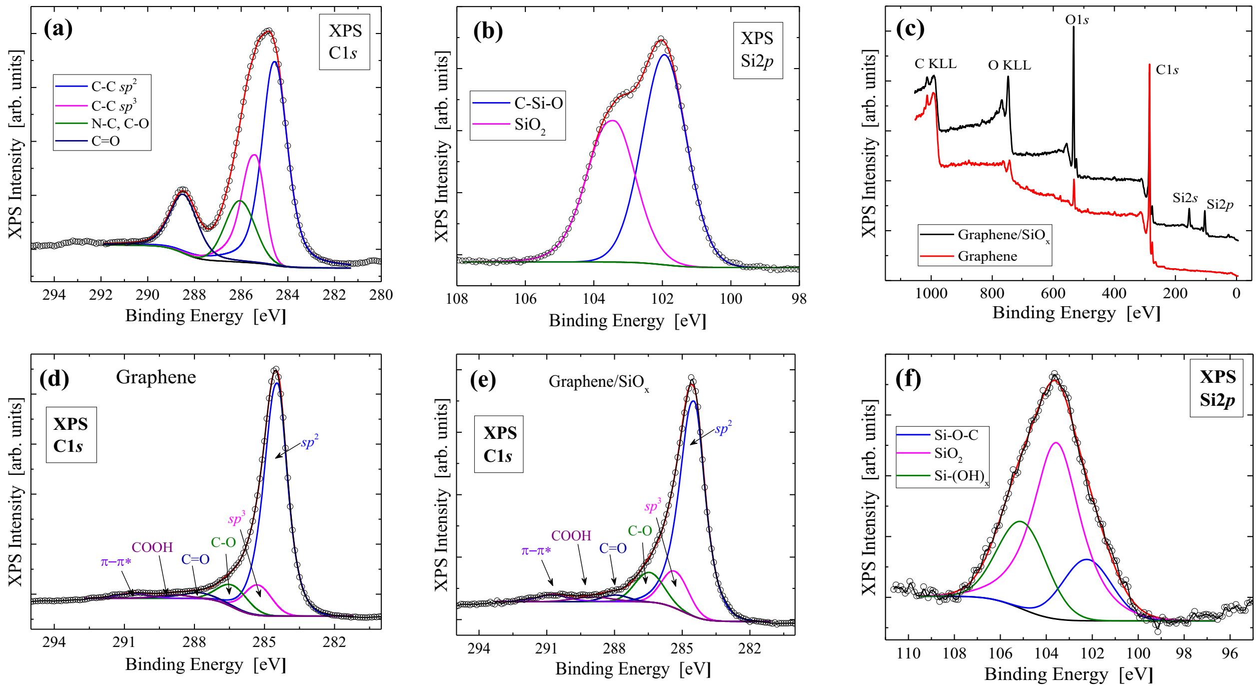

Fig. 5 Analysis of X-ray photoelectron spectra. Analysis of **a** C1*s* from neat PI and **b** Si2*p* from the silicone adhesive. **c** Survey scans of the laser-assisted produced graphene and graphene/SiO_x materials. Analysis of XP spectra of the C1*s* peak of **d** graphene and **e** graphene/SiO_x. **f** Analysis of the Si2*p* component of the graphene/SiO_x nanohybrid.

A detailed analysis of the chemical bonding of the graphene films has been carried out by X-ray photoelectron spectroscopy (XPS). Survey scans of the films, Supplementary Fig. 6a, reveal the existence of C/O/N elements for the neat PI foil. C/O/Si elements are found for the PI/silicone adhesive material measured from the side of the silicone adhesive, which justifies the absence of the N1*s* peak from the survey spectrum of the Kapton tape, due to the large thickness of the silicone adhesive film, i.e., ~35 μm. The C1*s* XPS peak of the Kapton foil, Fig. 5a, is analyzed into four components assigned to C–C sp^2, C–C sp^3, C–N/C–O, and C=O bonds. The binding energies and the relative concentration of these components are shown in Supplementary Tables 1 and 2, respectively. The N1*s* peak, Supplementary Fig. 6b, centered at 400.6 eV, is assigned to N–C bonds[42]. The Si2*p* XPS peak of the silicone adhesive (Kapton tape), Fig. 5b, is analyzed into two components assigned to C-Si-O[43], and to SiO_2 species[44]. The C1*s* peak, Supplementary Fig. 6c, consists of one peak at 284.5 eV characteristic of carbon bonding in PDMS[43].

Survey spectra of the laser-assisted decomposed products, LEST-F-74 and LEST-T-74, are shown in Fig. 5c. The almost complete absence of Nitrogen (<0.5 ± 0.1 at. %) demonstrates a very efficient laser-induced decomposition of the polyimide structure to elemental graphitic carbon. Each of the deconvoluted C1*s* peaks of the LEST-F-74 and LEST-T-74, illustrated in Fig. 5d, e, consists of six components. The relevant binding energies (BE) and the assignments of these components to various species[14] are compiled in Table 1. The relative fractions of the various species are similar for the C1*s* peak of the graphene and graphene/SiO_x films. A very high degree of sp^2 carbon atoms emerges, in relation to the sp^3 bonded ones, after decomposition. The π-π* satellite peak (at ~291 eV) is characteristic of aromatic carbon structures. Its appearance in the XP spectra, in relation to the very high sp^2 hybridization indicates an increased delocalized π conjugation structure of the decomposed materials. The analysis of XP spectra shows that Si-O-C bonding is highly likely to exist in the graphene/SiO_x films obtained by PI/silicone decomposition. However, the fraction of this species cannot be accurately determined because their BE emerges at ~286.2 eV[18], which coincides with the BE of the epoxy groups. The deconvolution of the Si2*p* XPS peak, of the graphene/SiO_x films, is presented in Fig. 5f, which shows that three components constitute this composite peak. The peak at 103.5 eV has unequivocally been assigned to stoichiometric silica, SiO_2, where Si has the +4 oxidation state[44]. The peak at 102.2 eV corresponds to Si oxidation state +3 and can be associated with Si-C bonds in tetrahedral species of the type O_3-Si-C[18]. The peak at the higher BE is related to $Si(OH)_x$ species[45], with x estimated to be in the range $1.5 < x \leq 2$ according to current data. The fractions of the Si atoms participating in these three different environments (Table 1) have been estimated using the total areas of the C1*s*, O1*s*, and Si2*p* peaks weighted by the relevant sensitivity factors and the transmission function of the energy analyzer. Combining the results of Si2*p* analysis (Table 1) with the total Si at. % (Table 2) we estimate that ~26.6% is the fraction of the O atoms. The larger part of O atoms, which correspond to ~24.6% of the total atoms, are bonded to Si. The remaining, ~2% of O atoms, bond to C atoms, yielding an atomic ratio of C/O ≈ 30 for the graphene/SiO_x

Table 1. Relative (%) atomic concentration of C and Si species.

	C1s		Si2p	
Component/ BE (±0.1 eV)	Graphene [± 0.5 %]	Graphene/ SiO_x [± 0.5 %]	Component/ BE (±0.1 eV)	Graphene/SiO_x [± 1.0 %]
C–C sp^2/284.5	75.1	71.4	-Si-O-C- 102.1	18.1
C–C sp^3/285.4	10.4	11.6		
C–O/286.5	8.0	10.1	SiO_2 103.4	56.2
C=O/287.9	3.4	2.1		
COOH/289.3	1.4	2.1	Si-$(OH)_x$, x≈2 104.9	25.7
π–π* satellite /~291	1.7	2.7		

Table 2. Relative (%) atomic concentration of O, Si, and C and C/O ratio derived from the XPS analysis.

	Graphene	Graphene/SiO$_x$ (at. %)
C	96.8 ± 0.1	59.5 ± 0.1
O	3.2 ± 0.1	26.6 ± 0.1 [~24.6 Si-O + ~2.0 C-O]
Si	–	13.9 ± 0.1
C/O	30.25	29.75

film (PI/silicone precursor), which is the same with the C/O ratio of the graphene film (PI precursor).

The LEST method was applied to other classes of carbon sources demonstrating that successful transfer can also take place for a wide class of materials. Supplementary Fig. 7 illustrates representative Raman spectra and SEM images of other carbon source materials, such as phenol-based resins and biomass-derived products, (i.e., homogenates of raisins). In addition, using a substrate that is transparent to the laser wavelength and placing this substrate between the laser beam and the target material (carbon source), we have exploited the backward LEST process. In this configuration, graphene flakes produced by the LEST mechanism is transferred backwards and becomes deposited on the transparent substrate. Supplementary Fig. 8 illustrates FE-SEM images of backward LEST graphene, using polyimide as the carbon source and a silica substrate as the transparent substrate.

Following the detailed morphological and physico-chemical analysis which enables the comprehension of the materials composition and structure, the merits of the LEST graphene-based films have been tested in the frame of two energy-conversion applications related to power sources, namely TENGs and supercapacitors.

Fabrication and performance evaluation of TENG devices

Early research efforts on miniaturized electromagnetic generators to harvest vibrational energy have paved the way towards the development of self-powered sensors and relevant devices[46]. The first TENG devices have been envisaged and fabricated by Wang and co-workers[47]. The working principle is based upon the coupling between electrostatic induction and contact electrification[48]. Bringing in contact two different materials, preferably selected from opposite sides of the triboelectric scale[49,50] generates on their surfaces static charges of opposite sign as a result of contact electrification. The charges can be collected by electrodes attached to the back side of the tribo-materials, creating a potential difference upon separating the materials. The performance (output power) and long-term stability of TENGs depends upon the choice of proper materials and the device structure[51]. Apart from contact-separation mode several other have been proposed including in-plane sliding, single-electrode, and free-standing triboelectric-layer modes[51].

Graphene-related materials have been used in various parts of TENG devices. Transparent TENGs were fabricated by CVD-grown graphene which was transferred on PET where few-layer graphene had the dual role of tribo-material and electrode[52]. In addition to the complicated steps followed for device fabrication, a rather limited open circuit voltage, V_{OC}, and short-circuit current density, J_{SC}, were obtained. Comparable results were obtained by a similar method, which took advantage of a water-based approach to achieve delamination of CVD graphene grown by a roll-to-roll process and transfer onto plastic substrate[53]. In an alternative approach, laser-grown graphene on polyimide and cork was used as the electrode of a TENG device with a dielectric-to-conductor structure[54]. It was also shown that flexible/stretchable devices can be prepared by transferring graphene grown on Kapton to PDMS using, however, an elaborate method entailing many steps, which may affect the integrity of the GRM film.

Here, we employ a single-electrode TENG device architecture implemented by the LEST of graphene and graphene/SiO$_x$ hybrids on PDMS substrate. A fairly low sheet resistance of the graphene film and its ability to withstand several cycles of operation are key factors towards replacing the precious metals deposited on the back side of the contact material[48]. To demonstrate the potential of the flexible, wearable TENG devices fabricated by the process developed in the current work, the single-electrode construction adopted here employs PDMS and human skin as active tribo-materials. The schematic design of the TENG devices prepared in this work, are shown in Fig. 6a. The proposed method is simpler than previously reported works, where multi-step processes are involved to transfer of graphene from Kapton on PDMS, i.e. by mold-casting the PDMS on the graphitized side of Kapton and peeling off the Kapton foil[54]. The active area of the device is 1 × 2 cm^2. Trains of the open circuit voltage, generated by tactile motion (finger tapping) imposed on the PDMS for the neat graphene electrode and the electrode of the graphene/SiO$_x$ nanohybrid, are displayed in Fig. 6b, c. The normal force applied in this way is typically in the range 0.2–1.0 N[55]. The comparison reveals that the average peak-to-peak V_{OC} induced by the PDMS/human skin-based TENG lies within the range of 50–60 V for the device employing neat graphene as the electrode (LEST-F-74), whereas it almost halves, ~30 V, when the nanohybrid graphene/SiO$_x$ (LEST-T-74) is used as the electrode material. The irregularity of the peak maxima reflects the fact that the signal has not been measured using a constant force generated by a vibrating motorized machine, but by means of finger tapping, as mentioned above. This simulates more realistically vibrational (biomechanical) energy generated by the human body. The experiments were reiterated several times providing a very high degree of repeatability. Long-term tests reaching 5000 cycles over a period of few months showed a decrease of the V_{OC} of ~ 50%. Despite that the TENG devices was not treated under protective conditions they exhibited high stability and integrity being able to light at least eight green LEDs by finger tapping (see Supplementary Fig. 9 and Supplementary Video). This result demonstrates that graphene-like and graphene/SiO$_x$ films prepared by LEST on PDMS overcome issues, i.e. adhesion and atmospheric effects, which is a main concern in the case of electrodes made of vacuum-deposited metallic films on PDMS.

The output power of the TENG device has been determined by adding various load resistors, ranging from 1 to 100 MΩ, and measuring the output voltage, V_{output} and I_{SC} as shown in Fig. 6d, e. A better response, as regards both these two parameters, is observed for the device prepared by the graphene/SiO$_x$ nanohybrid in comparison to that incorporating neat graphene film. This is more quantitatively reflected in the generated power per unit area, P^A_{out}, depicted in Fig. 6f for the two types of devices. The instantaneous P^A_{out} is ~82 and ~110 mW m^{-2} for the TENGs using graphene and graphene/SiO$_x$, respectively. This is obtained when the load resistance is $R^L \approx 3$ MΩ for both TENG devices. Based on the principle of maximum power transfer, the output power from an energy device, such as the TENG, coupled to an external load, is maximized when the internal impedances of the device and the load are equal. As Fig. 6 reveals, the V_{OC} of the Kapton foil electrode is higher than that of the Kapton tape. However, the instantaneous outpower power of the device prepared by Kapton foil is slightly lower than that prepared by Kapton tape. A possible reason is that the different sheet resistance of the two electrodes could influence the observed behavior. Indeed, films prepared by the Kapton tape tend to exhibit lower sheet resistance than films of graphene prepared using the Kapton foil. The difference in sheet resistance of the electrodes is responsible for the somewhat higher short circuit current values in the case of the Kapton tape,

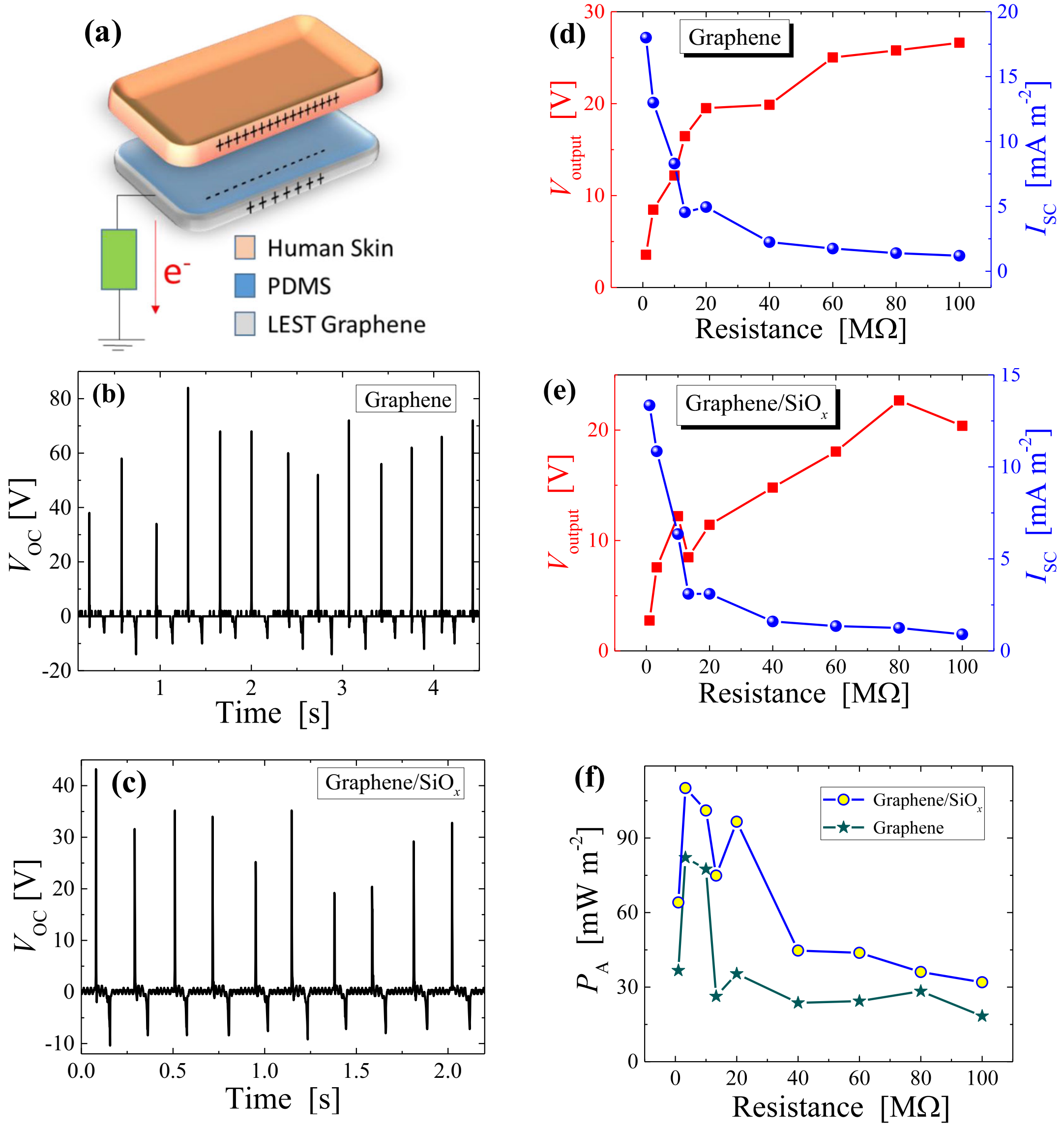

Fig. 6 Performance of TENGs devices. a Schematic of the structure of the single-electrode TENG device. **b**, **c** V_{oc} generated during contact and separation of PDMS with human skin with graphene and graphene-SiO$_x$ nanohybrid as electrode, respectively. **d**, **e** Output voltage and short circuit current (I_{SC}) generated upon different external load resistors. **f** Output power density of the TENG devices as a function of the load resistance.

Fig. 6d, which in turn provided slightly higher values in the instantaneous output power.

A remarkable finding of this work is that the external resistance value providing maximum output of the TENG, R^L_{max}, is among the lowest reported in the literature. Given the high impedance of other reported TENGs, this is a significant advantage of the current device, considering that the reduction of the internal impedance is highly desirable in a number of devices requiring low impedance loads for many practical applications[56]. A detailed investigation on the conditions of P^A_{out} in TENGs has shown that the value of the R^L_{max} decreases proportionally with the frequency of the force applied to the TENG device[56]. This is a very significant result, as the implementation of high frequency TENG operation in wearable electronics is practically limited in several application to physical constraints. Apparently, the current design emerges as a promising solution towards realizing tactile sensors and other components embedded in electronic textiles.

Theoretical modeling of TENG operation has shown that R^L_{max} and P^A_{out} depend upon the film thickness of the tribo-material[56]. The lower the thickness, the lower the R^L_{max}; whereas, the opposite trend holds for the P^A_{out}. More dramatic effects have been observed when increasing the TENG area (lateral dimensions). This causes significant increase of the P^A_{out} and appreciable decrease of the that R^L_{max}. Considering the above criteria of TENG operation optimization, it is evident that the low PDMS thickness (200 μm) and lateral dimensions (1 × 2 cm^2) used in our devices leave room for improvement by further tuning the TENG parameters.

Fabrication and performance evaluation of supercapacitors

The performance of the two types of graphene-based electrodes was also explored in electrochemical energy storage applications. In this case, a carbon paper (180 μm thick) served as the substrate onto which graphene and graphene/SiO$_x$ films were deposited by LEST of both precursors, i.e., Kapton foil and tape, respectively. Since the obtained deposited films differ substantially in terms of weight, various laser-assisted deposition steps were considered.

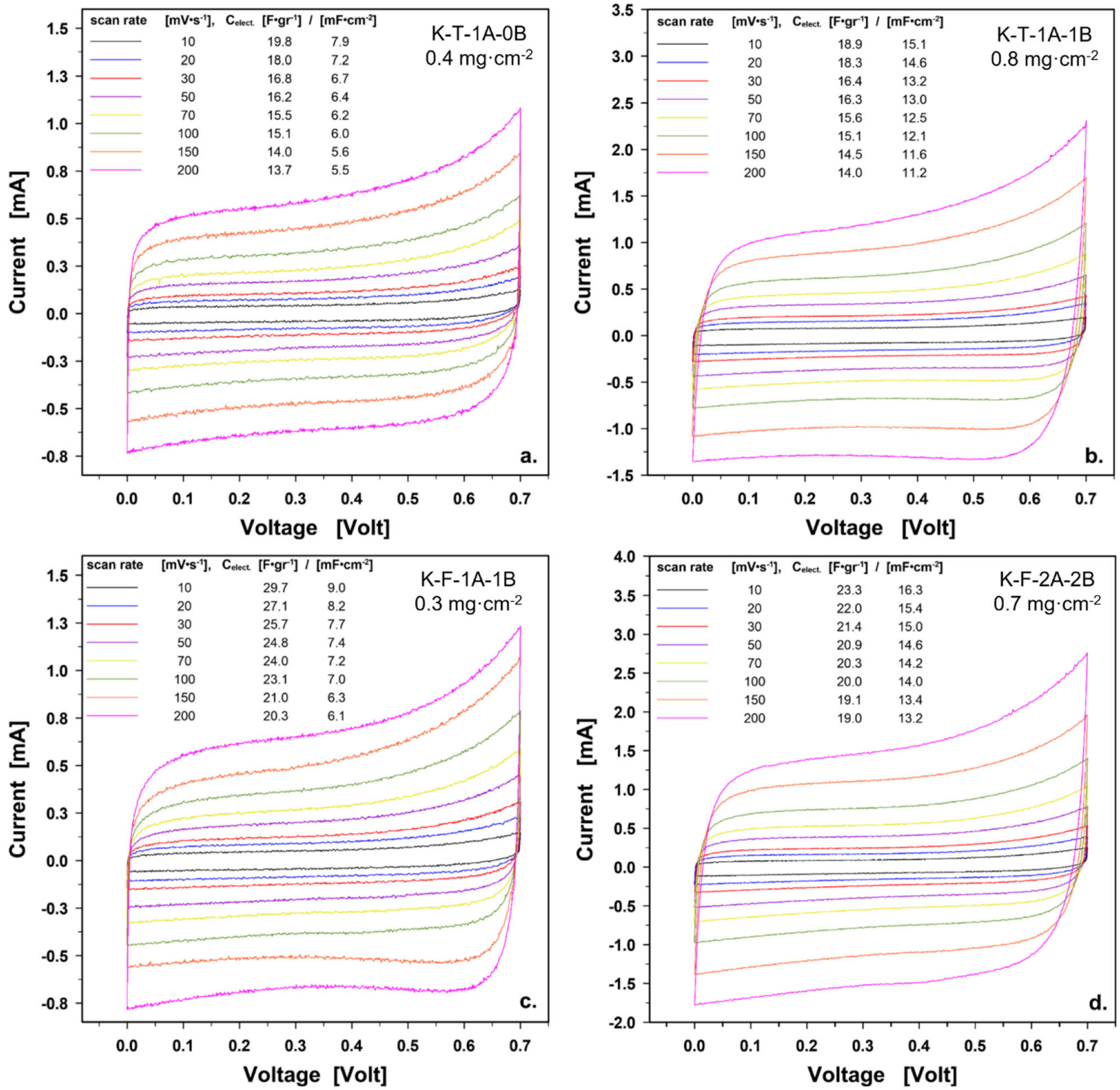

Fig. 7 **Performance of supercapacitors.** CV curves at different scan rates for the supercapacitors prepared by four different electrodes of variable loading. Neat graphene flakes electrodes: **a** K-T-1A-0B, **b** K-T-1A-1B. Graphene/SiO$_x$ electrodes: **c** K-F-1A-1B, **d** K-F-2A-2B. See text for sample description.

The Kapton tape precursor led to higher yield and was applied in the following schemes. (i) Precursor: PI/silicone adhesive; single deposition on the one side of carbon paper. (ii) Precursor: PI/silicone adhesive; single deposition on both sides of carbon paper. (iii) Precursor: PI; single deposition on both sides of carbon paper. Two-sided deposition was required to attain mass loading similar to case (i), so as to provide a rational comparison of the gravimetric specific capacitance between the two materials. (iv) Precursor: PI; double deposition on both sides of carbon paper. Four depositions (two per side) were required to attain mass loading similar to case (ii), so as to provide a rational comparison of the gravimetric specific capacitance between graphene and graphene/SiO$_x$. In each case, a pair of identical electrodes were produced which were used to fabricate a series of symmetrical supercapacitors in the form of Swagelok type cells. The sample notation is K-(T/F)-xA-yB, where K stands for Kapton, T/F denotes tape/foil, $x = 1{,}2$, $y = 0{,}1{,}2$ show the number of depositions, while A and B stand for the top and bottom side of the carbon paper (current collector). The four cases described above are symbolized as (i) K-T-1A-0B, (ii) K-T-1A-1B, (iii) K-F-1A-1B, and (iv) K-F-2A-2B.

The corresponding cyclic voltammograms (CVs) at various scanning rates (10–200 mV s^{-1}) for the above four types of supercapacitors are depicted in Fig. 7a–d. In all cases, a quasi-rectangular CV shape is obtained and it is attributed to the electric double-layer capacitance (EDLC) nature of these graphene-based electrodes. On the other hand, a narrow working voltage window was achieved (ca. 0.7 V), which limits their specific energy potential and thus their overall performance. Above this voltage an abrupt increase of current is observed, most probably due to gas evolution, which is a well-documented aging phenomenon in EDLC devices[57]. Although water-splitting (described by the two half-reactions: hydrogen and oxygen evolution) is the most prominent pathway of cell degradation, it is not the only one. Parallel phenomena may also intervene[57], such as electrochemical gas consumption, carbon corrosion, and carbon surface functional groups decomposition (e.g., oxygenated groups)[58]. Such contributions may explain the observed narrowing of the working voltage window limit of all cells, from the expected value, ~1 V, of a conventional aqueous symmetric EDLC device. In addition, several other factors can affect the operating voltage window of a supercapacitor; namely, the electrodes mass ratio and/or its surface charge[59]. In particular mass-balancing of electrodes is a key factor to manipulate the voltage window[60,61], otherwise an imbalance can lead to unfavorable restrictions to the maximum achieved voltage range[61].

Assuming an ideal EDLC behavior as evinced by the symmetric and almost rectangular CV plots, the gravimetric specific (C_{gr}) and areal (C_{ar}) capacitance of the electrodes are calculated using the set of Supplementary Equations (1)–(4). It is observed that using a single lase pass on a carbon paper surface, the loading of graphene/SiO_x electrodes is almost twice as that of neat graphene. Therefore, increased precursor mass and longer process time (two laser passes) are required for the PI foil to achieve the same areal capacitance as that obtained by the PI/silicone tape. On the other hand, the graphene/SiO_x electrodes yield an overall decreased gravimetric specific capacitance, in relation to the graphene electrodes, prepared using the same lasing procedure/steps. Indicatively, depending upon the scan rate, the calculated specific capacitance C_{gr} of graphene electrode is found to be 30–50% higher than that of the graphene/SiO_x electrode, see Fig. 7b, c, despite that the latter electrode exhibits a BET surface area higher than that of the graphene electrode by ~40%, Supplementary Fig. 10. The lower specific capacitance of the graphene/SiO_x nanohybrid can be attributed to the presence of SiO_x particles, which could either decrease the specific surface area by changing the porosity of the graphene film or block sites amenable to charge/discharge processes. Analyzing the pore size distribution shown in Supplementary Fig. 10, it is evident that the main difference between the two materials, is the complete absence of mesopores with radii in the range of 3–6 nm for the graphene/SiO_x material. This finding suggests that the presence of SiO_x nanoparticles and the way that they are structured together with the graphene flakes, changes the porosity of the film, by blocking a fraction of useful carbon sites, preventing the translocation of the electrolyte's ions to those sites.

Another possible explanation for the lower C_{gr} of the graphene/SiO_x electrode could be related to the fact that the C_{gr} is somewhat underestimated, because SiO_x weight is considered in the electrode material weight, while its activity in EDLC applications is expected to be much inferior to that of graphene. Even so, a few existing studies claim that SiO_2 addition may be beneficial in supercapacitor applications. For example, the incorporation of SiO_2 has been reported to positively affect the microstructure and charge–discharge performance of reduced graphene composites in polyaniline-based supercapacitors[62]. Further, it has been shown that proper loading and size of SiO_2 nanoparticles dispersed into the electrode matrix may improve the electrode/electrolyte affinity, hence contributing positively to the performance of a EDLC supercapacitor)[63]. The capacitance of the graphene electrodes was also calculated by analyzing the galvanostatic charge-discharge (GCD) curves, shown in Supplementary Fig. 11. Based on the almost triangular shape of the curves, equations SE5 and SE6 (Supplementary information) have been applied. The remarkable gravimetric capacitance retention (CR) of both graphene and graphene/SiO_x electrodes (compared at similar lasing passes) is depicted in Supplementary Fig. 12 as a function of the scan rate (v) and discharge current I_d. All four devices exhibit good rate performance as can be seen in Supplementary Fig. 12, with capacitance retention vs. I_d being 80% or higher, whereas the K-F-2A-2B device exhibits the best retention, namely, ~97% vs. discharge current and ~82% vs. scan rate.

Overall, graphene/SiO_x outperforms neat graphene electrode as far as areal capacitance is concerned; whereas, the opposite holds when the specific capacitance (gravimetric) is compared. In addition, considering the more efficient single pass loading of the electrode by graphene/SiO_x and its better adhesion on the carbon paper in relation to graphene, renders this nanohybrid material a better choice for electrochemical energy storage.

In summary, we have presented a laser-based physical method, LEST, of growing and simultaneously transferring turbostratic graphene flakes and graphene-based nanohybrids on any type of substrate. An industrial-type laser has been used to decompose various carbon sources (polymers, biomass), with the emphasis being placed on the case example of PI and PI/silicone adhesive, to prepare films of graphene flakes and graphene/SiO_x nanohybrids. The process developed in this work operates at ambient environment using single lase mode at large irradiation spot diameter (a few mm). These conditions advocate for the scalability of the method to an industrial scale. A detailed morphological and spectroscopic analysis has revealed the formation of sponge-like graphene with high specific surface area and low sheet resistance. In the case of the graphene/SiO_x nanohybrid, HR-TEM showed a narrow particle size distribution of silicon oxide nanoparticles in the scale < 50 nm, which are wrapped around by graphene layers. A worth-noting finding of Raman scattering and HR-TEM, pertains to the turbostratic stacking of the graphene structure, which arises as a scarce but very beneficial attribute of laser-assisted graphene, due to electronic decoupling of the layers. XPS analysis has shown a very high C/O ratio, ~30, in the laser-decomposed products, for both neat graphene flakes and graphene/SiO_x. A rich Si environment was revealed by XPS, quantified as -Si-O-C-, Si-$(OH)_x$ with $x \approx 2$ and SiO_2, with the latter representing almost 60% of the Si species.

The excellent features of the obtained films of graphene flakes and graphene/SiO_x nanohybrids has allowed the development of electrodes deposited directly by LEST onto PDMS and carbon fiber paper for the evaluation performance of TENG and EDLC devices, respectively. A simple construction of single electrode TENG device was constructed and its output power against soft finger tapping was assessed. The maximum P^A_{out} was estimated to be ~82 and ~110 mW m^{-2} for the TENGs using graphene and graphene/SiO_x, respectively. Perhaps the most important finding is that these values have been obtained for load resistance $R^L \approx 3$ MΩ. This remarkable result demonstrates that the single electrode TENG devices constructed here present one of the lowest reported impedance of similar devices. Both electrodes exhibit very competitive capacitance as estimated by analyzing CV curves and galvanostatic charge-discharge curves. Concerning the areal capacitance value, the graphene/SiO_x electrode was found to outperform the neat graphene electrode; whereas, the graphene electrode demonstrated outstanding capacitance retention vs I_d of about 97%. Based on the strong adhesion and the more efficient single pass laser-assisted loading of the electrode by graphene/SiO_x, we anticipate the nanohybrid material as a more efficient alternative of graphene for electrochemical energy storage.

Concluding, the current approach is generic. It is applicable to a number of several other precursors, such as organic, polymer, biomass waste, and so on. Currently, we demonstrate that various precursors can be incurred into a simultaneous decomposition and transformation towards high-purity turbostratic graphene porous matrix and its deposition on various substrates relevant to a number of applications. In this frame, the LEST method advanced here, encompassing the laser-assisted graphene formation and transfer, emerges as a paradigm of additive manufacturing for graphene-based devices. The inherent scalability of the LEST method can be exploited to advance a technology capable of bridging the gap between academic research and industrial manufacturing in graphene-based nanohybrids materials.

METHODS

Laser-assisted deposition of porous graphene films

The laser-assisted decomposition of the Kapton materials took place with the use of an Nd:YAG laser operating at 1064 nm operating with long pulses in the ms time scale. The pulse duration selected for the current experiment is 1.5 ms. All irradiation steps were performed at single laser mode. The Kapton foil used was 70 µm thick, while the Kapton tape, (RS Components product # 171-1615) was 65 µm thick, composed of a 35 µm thick silicone-based adhesive and a 30 µm thick Kapton film. The Kapton precursors were irradiated using overlapping pulses (50%) with a large spot size of about 1.5 mm in diameter. Laser parameters were optimized to attain optimum conditions for the transformation of carbon precursors to high-purity turbostratic few-layer graphene structures. Using a motorized x-y stage, the transfer area for graphene film on the acceptor substrate was selected according to the application requirement. The working area was $1 \times 2\,\mathrm{cm}^2$ for the TENG electrode, while areas of continuous graphene films of $1.5 \times 4\,\mathrm{cm}^2$ were processed for the supercapacitor electrodes. To optimize the graphene purity and quality, the laser fluence was varied in the range from 13 to 186 $\mathrm{J\,cm}^{-2}$. Various tests were performed, where the target materials were placed in certain distances (ranging from sub-mm to few mm) from the substrate to ensure both a homogeneous coverage and good adhesion of the graphene film on the substrate. However, because the $\mathrm{R_s}$ values exhibit slight differences in relation to the gap distance, the value of the latter was chosen to be ~0.5 mm (lower R_s) for all depositions that took place in the current work. Films of different precursors (resins and biomass-derived products) were prepared by drop casting of a suitable suspension (phenol resin/aqueous mixture of blended raisins) on a glass substrate which was then subjected to the LEST process.

Characterization of physico-chemical properties

The texture and morphology of the GRM-based films were investigated with the aid of a high-resolution field-emission scanning electron microscope (FE-SEM) instrument (Zeiss, SUPRA 35VP) operating at 10 kV. The microstructure of the graphene-based materials was examined utilizing a high-resolution field emission transmission electron microscope (Thermo Fisher Scientific, Talos F200i) operating at 200 kV. TEM specimens were prepared by drop casting 5 µl of aqueous suspension of the materials onto holey carbon support copper TEM grids. X-Ray diffraction data were recorded using a Bruker D8 Advance system with a nickel filtered CuKa anode ($\lambda = 1.5406$ Å) operating at 40 kV and 40 mA. Raman spectra were recorded with the 514.5 nm laser line using a laser power lower than ~1.5 mW. A micro-Raman spectrometer (T-64000, Jobin Yvon) was employed to analyze the scattered light, while a microscope objective of 50× magnification was used to focus and collect scattered light, resulting in a spot size of 2–3 µm. The Raman shift was calibrated using the Raman band of crystalline Si at ~520 cm^{-1}. Sheet resistance measurements were conducted with a four-point probe system (Ossila).

X-ray photoelectron spectroscopy was performed in UHV ($P \sim 5 \times 10^{-10}$ mbar) system equipped with a hemispherical electron analyzer (SPECS, Phoibos 100-1D-DLD) and a non-monochromatized dual-anode Mg/Al x-ray gun. Wide-survey and narrow scans of C 1*s*, O 1*s* and Si 2*p* spectra were recorded with using the x-ray source MgKα at 1253.6 eV photon energy and an analyzer pass energy of 10 eV giving a Full Width at Half Maximum (FWHM) of 0.85 eV for the Ag3*d*5/2 line. Spectra were accumulated and fitted using commercial software (SpecsLab Prodigy; Specs GmbH, Berlin). The XP core level peaks are deconvoluted with a mixed Gaussian–Lorentzian functions after a Shirley background subtraction. The graphitic powders were directly deposited on Mo foil by LEST.

TENG device fabrication and performance evaluation

Single-electrode, human touch, triboelectric nanogenerators were prepared using a thick film of PDMS as the active tribo-material. Both types of polyimide (Kapton foil and tape) were decomposed and deposited on PDMS. The graphene and graphene/$\mathrm{SiO_x}$ films are highly conductive and serve as the electrodes for collecting the generated carriers. The TENG device was encapsulated with Kapton tape from one side to secure the graphene electrode and to ensure good connection between graphene electrodes with connecting wire. Voltage peaks were generated by soft finger tapping of the PDMS at a non-constant frequency to simulate random body motion. The generated V_{OC} was measured with the aid of a digital oscilloscope (Tektronics TBS1052B-EDU). Short-circuit current was measured across a range of external load resistors (1–100 MΩ).

Supercapacitor assembly and electrochemical measurements

The electrochemical performance of the graphene-based materials was conducted by investigating their performance in a two-electrode supercapacitor device. The active materials were deposited in the form of graphene-like films to a suitable current collector in order to fabricate two identical electrodes. Sigracet 29AA non-woven carbon fiber paper (PTFE-free) of 190 µm thickness served as current collector while a Dreamweaver Titanium T 0.58/30 (GLATFELTER) membrane of 30 µm thickness was used as a separator. The final symmetric supercapacitor (1.1 cm^2 total electrode area) was assembled in the form of a Swagelok type cell and filled with 6 M KOH electrolyte. All electrochemical measurements were acquired with an Autolab PGSTAT302 N potentiostat/galvanostat.

DATA AVAILABILITY

The data that support the findings of this study are available from the corresponding author upon reasonable request.

Received: 4 October 2021; Accepted: 13 July 2022;

REFERENCES

1. Allen, M. J., Tung, V. C. & Kaner, R. B. Honeycomb carbon: a review of graphene. *Chem. Rev.* **110**, 132–145 (2010).
2. Castro Neto, A. H., Guinea, F., Peres, N. M. R., Novoselov, K. S. & Geim, A. K. The electronic properties of graphene. *Rev. Mod. Phys.* **81**, 109–162 (2009).
3. Schwierz, F. Graphene transistors. *Nat. Nanotechnol.* **5**, 487–496 (2010).
4. Ferrari, A. C. et al. Science and technology roadmap for graphene, related two-dimensional crystals, and hybrid systems. *Nanoscale* **7**, 4598–4810 (2015).
5. Segal, M. Selling graphene by the ton. *Nat. Nanotechnol.* **4**, 612–614 (2009).
6. Zurutuza, A. & Marinelli, C. Challenges and opportunities in graphene commercialization. *Nat. Nanotechnol.* **9**, 730–734 (2014).
7. Kauling, A. P. et al. The worldwide graphene flake production. *Adv. Mater.* **30**, 1803784 (2018).
8. Yannopoulos, S. N. et al. $\mathrm{CO_2}$-laser-induced growth of epitaxial graphene on 6H-SiC(0001). *Adv. Funct. Mater.* **22**, 113–120 (2012).
9. Antonelou, A., Dracopoulos, V. & Yannopoulos, S. N. Laser processing of SiC: From graphene-coated SiC particles to 3D graphene froths. *Carbon* **85**, 176–184 (2015).
10. Lin, J. et al. Laser-induced porous graphene films from commercial polymers. *Nat. Commun.* **5**, 5714 (2014).
11. Samartzis, N., Athanasiou, M., Dracopoulos, V., Yannopoulos, S. N. & Ioannides, T. Laser-assisted transformation of a phenol-based resin to high quality graphene-like powder for supercapacitor applications. *Chem. Eng. J.* **430**, 133179 (2021).
12. Chyan, Y. et al. Laser-induced graphene by multiple lasing: toward electronics on cloth, paper, and food. *ACS Nano* **12**, 2176–2183 (2018).
13. Athanasiou, M. et al. High-quality laser-assisted biomass-based turbostratic graphene for high-performance supercapacitors. *Carbon* **172**, 750–761 (2021).
14. Antonelou, A., Sygellou, L., Vrettos, K., Georgakilas, V. & Yannopoulos, S. N. Efficient defect healing and ultralow sheet resistance of laser-assisted reduced graphene oxide at ambient conditions. *Carbon* **139**, 492–499 (2018).
15. Sokolov, D. A., Shepperd, K. R. & Orlando, T. M. Formation of graphene features from direct laser-induced reduction of graphite oxide. *J. Phys. Chem. Lett.* **1**, 2633–2636 (2010).
16. Antonelou, A., Benekou, V., Dracopoulos, V., Kollia, M. & Yannopoulos, S. N. Laser-induced transformation of graphitic materials to two-dimensional graphene-like structures at ambient conditions. *Nanotechnology* **29**, 384001 (2018).
17. Kumar, R. et al. Laser-assisted synthesis, reduction and micro-patterning of graphene: Recent progress and applications. *Coord. Chem. Rev.* **342**, 34–79 (2017).
18. Yang, L., Wang, L., Xing, M., Lei, J. & Zhang, J. Silica nanocrystal/graphene composite with improved photoelectric and photocatalytic performance. *Appl. Catal. B Environ.* **180**, 106–112 (2016).
19. Watcharotone, S. et al. Graphene-silica composite thin films as transparent conductors. *Nano Lett.* **7**, 1888–1892 (2007).
20. Niu, F., Liu, J.-M., Tao, L.-M., Wang, W. & Song, W.-G. Nitrogen and silica co-doped graphene nanosheets for $\mathrm{NO_2}$ gas sensing. *J. Mater. Chem. A* **1**, 6130 (2013).

21. Cao, M. et al. Graphene nanohybrids: excellent electromagnetic properties for the absorbing and shielding of electromagnetic waves. *J. Mater. Chem. C* **6**, 4586–4602 (2018).
22. Serra, P. & Piqué, A. Laser-induced forward transfer: fundamentals and applications. *Adv. Mater. Technol.* **4**, 1800099 (2019).
23. Smits, E. C. P., Walter, A., de Leeuw, D. M. & Asadi, K. Laser induced forward transfer of graphene. *Appl. Phys. Lett.* **111**, 173101 (2017).
24. Komlenok, M. S. et al. Printing of crumpled CVD graphene via blister-based laser-induced forward transfer. *Nanomaterials* **10**, 1103 (2020).
25. Praeger, M. et al. Laser-induced backward transfer of monolayer graphene. *Appl. Surf. Sci.* **533**, 147488 (2020).
26. Papazoglou, S. et al. A direct transfer solution for digital laser printing of CVD graphene. *2D Mater.* **8**, 045017 (2021).
27. Srinivasan, R., Hall, R. R., Wilson, W. D., Loehle, W. D. & Allbee, D. C. Ultraviolet laser irradiation of the polyimide, PMDA-ODA (Kapton^{TM}), to yield a patternable, porous, electrically conducting carbon network. *Synth. Met.* **66**, 301–307 (1994).
28. Srinivasan, R., Hall, R. R., Loehle, W. D., Wilson, W. D. & Allbee, D. C. Chemical transformations of the polyimide Kapton brought about by ultraviolet laser radiation. *J. Appl. Phys.* **78**, 4881–4887 (1995).
29. Ortelli, E. E., Geiger, F., Lippert, T., Wei, J. & Wokaun, A. UV-laser-induced decomposition of Kapton studied by infrared spectroscopy. *Macromolecules* **33**, 5090–5097 (2000).
30. Taylor, R. S., Leopold, K. E., Singleton, D. L., Paraskevopoulos, G. & Irwin, R. S. The effect of debris formation on the morphology of excimer laser ablated polymers. *J. Appl. Phys.* **64**, 2815–2818 (1988).
31. Singleton, D. L., Paraskevopoulos, G. & Irwin, R. S. XeCl laser ablation of polyimide: Influence of ambient atmosphere on particulate and gaseous products. *J. Appl. Phys.* **66**, 3324–3328 (1989).
32. Srinivasan, R. & Braren, B. Ultraviolet laser ablation of organic polymers. *Chem. Rev.* **89**, 1303–1316 (1989).
33. Srinivasan, R., Braren, B. & Dreyfus, R. W. Ultraviolet laser ablation of polyimide films. *J. Appl. Phys.* **61**, 372–376 (1987).
34. von Gutfeld, R. J. & Srinivasan, R. Electrostatic collection of debris resulting from 193 nm laser etching of polyimide. *Appl. Phys. Lett.* **51**, 15–17 (1987).
35. Walkup, R. E., Jasinski, J. M. & Dreyfus, R. W. Studies of excimer laser ablation of solids using a Michelson interferometer. *Appl. Phys. Lett.* **48**, 1690–1692 (1986).
36. Dyer, P. E., Pervolaraki, M. & Lippert, T. Experimental studies and thermal modelling of 1064- and 532-nm Nd:YVO4 micro-laser ablation of polyimide. *Appl. Phys. A* **80**, 529–536 (2005).
37. Hass, J. et al. Why multilayer graphene on 4H−SiC(0001) behaves like a single sheet of graphene. *Phys. Rev. Lett.* **100**, 125504 (2008).
38. Lespade, P., Marchand, A., Couzi, M. & Cruege, F. Caracterisation de materiaux carbones par microspectrometrie Raman. *Carbon* **22**, 375–385 (1984).
39. Rao, R. et al. Effects of layer stacking on the combination raman modes in graphene. *ACS Nano* **5**, 1594–1599 (2011).
40. Cong, C., Yu, T., Saito, R., Dresselhaus, G. F. & Dresselhaus, M. S. Second-order overtone and combination Raman modes of graphene layers in the range of 1690−2150 cm^{-1}. *ACS Nano* **5**, 1600–1605 (2011).
41. Deprez, N. & McLachlan, D. S. The analysis of the electrical conductivity of graphite conductivity of graphite powders during compaction. *J. Phys. D. Appl. Phys.* **21**, 101–107 (1988).
42. Beamson, G. & Briggs, D. *The XPS of Polymers Database. Surface Spectra* (Wiley, 2000).
43. Louette, P., Bodino, F. & Pireaux, J.-J. Poly(dimethyl siloxane) (PDMS) XPS reference core level and energy loss spectra. *Surf. Sci. Spectra* **12**, 38–43 (2005).
44. Himpsel, F. J., McFeely, F. R., Taleb-Ibrahimi, A., Yarmoff, J. A. & Hollinger, G. in *The Physics and Chemistry of SiO$_2$ and the Si-SiO$_2$ Interface* 219–225 (Springer US, 1988). https://doi.org/10.1007/978-1-4899-0774-5_24
45. Oliveira, R. L., Oliveira, C. S., Landers, R. & Correia, C. R. D. Pd nanoparticles immobilized on graphene oxide/silica nanocomposite: efficient and recyclable catalysts for cross-coupling reactions. *Chem. Sel.* **3**, 535–543 (2018).
46. Beeby, S. P. et al. A micro electromagnetic generator for vibration energy harvesting. *J. Micromech. Microeng.* **17**, 1257–1265 (2007).
47. Fan, F.-R., Tian, Z.-Q. & Lin Wang, Z. Flexible triboelectric generator. *Nano Energy* **1**, 328–334 (2012).
48. Wang, Y., Yang, Y. & Wang, Z. L. Triboelectric nanogenerators as flexible power sources. *npj Flex. Electron.* **1**, 10 (2017).
49. Henniker, J. Triboelectricity in polymers. *Nature* **196**, 474 (1962).
50. Diaz, A. F. & Felix-Navarro, R. M. A semi-quantitative tribo-electric series for polymeric materials: the influence of chemical structure and properties. *J. Electrostat.* **62**, 277–290 (2004).
51. Zhou, Y., Deng, W., Xu, J. & Chen, J. Engineering materials at the nanoscale for triboelectric nanogenerators. *Cell Rep. Phys. Sci.* **1**, 100142 (2020).
52. Kim, S. et al. Transparent flexible graphene triboelectric nanogenerators. *Adv. Mater.* **26**, 3918–3925 (2014).
53. Chandrashekar, B. N. et al. Roll-to-roll green transfer of CVD graphene onto plastic for a transparent and flexible triboelectric nanogenerator. *Adv. Mater.* **27**, 5210–5216 (2015).
54. Stanford, M. G. et al. Laser-induced graphene triboelectric nanogenerators. *ACS Nano* **13**, 7166–7174 (2019).
55. Asakawa, D. S., Crocker, G. H., Schmaltz, A. & Jindrich, D. L. Fingertip forces and completion time for index finger and thumb touchscreen gestures. *J. Electromyogr. Kinesiol.* **34**, 6–13 (2017).
56. Dharmasena, R. D. I. G., Deane, J. H. B. & Silva, S. R. P. Nature of power generation and output optimization criteria for triboelectric nanogenerators. *Adv. Energy Mater.* **8**, 1802190 (2018).
57. He, M., Fic, K., Frąckowiak, E., Novák, P. & Berg, E. J. Ageing phenomena in high-voltage aqueous supercapacitors investigated by in situ gas analysis. *Energy Environ. Sci.* **9**, 623–633 (2016).
58. Kado, Y., Soneda, Y., Hatori, H. & Kodama, M. Advanced carbon electrode for electrochemical capacitors. *J. Solid State Electrochem.* **23**, 1061–1081 (2019).
59. Gou, Q., Zhao, S., Wang, J., Li, M. & Xue, J. Recent advances on boosting the cell voltage of aqueous supercapacitors. *Nano-Micro Lett.* **12**, 98 (2020).
60. Vaquero, S., Palma, J., Anderson, M. & Marcilla, R. Mass-balancing of electrodes as a strategy to widen the operating voltage window of carbon/carbon supercapacitors in neutral aqueous electrolytes. *Int. J. Electrochem. Sci.* **8**, 10293–10307 (2013).
61. Hu, L., Guo, D., Feng, G., Li, H. & Zhai, T. Asymmetric behavior of positive and negative electrodes in carbon/carbon supercapacitors and its underlying mechanism. *J. Phys. Chem. C* **120**, 24675–24681 (2016).
62. Wang, H. et al. Smart and designable graphene–SiO 2 nanocomposites with multifunctional applications in silicone elastomers and polyaniline supercapacitors. *RSC Adv.* **7**, 11478–11490 (2017).
63. Lo, A.-Y., Chang, C.-C., Lai, Y.-W., Chen, P.-R. & Xu, B.-C. Improving the supercapacitor performance by dispersing SiO$_2$ microspheres in electrodes. *ACS Omega* **5**, 11522–11528 (2020).

ACKNOWLEDGEMENTS

This research was partly supported by the project 'National Infrastructure in Nanotechnology, Advanced Materials and Micro-/ Nanoelectronics' (MIS 5002772) which is implemented under the Action Reinforcement of the Research and Innovation Infrastructure, funded by the Operational Programme Competitiveness, Entrepreneurship and Innovation (NSRF 2014-2020) and co-financed by Greece and the European Union (European Regional Development Fund). K.B. and S.N.Y. acknowledge support by the European Union's H2020 research and innovation programme under the Marie Skłodowska-Curie grant agreement N. 721642 (SOLUTION).

AUTHOR CONTRIBUTIONS

K.B., N.S., and S.N.Y. conceived the idea. K.B., N.S., and M.A. performed experiments and analyzed the data. L.S. performed the XPS experiment and provided data analysis. N.B. performed the TEM and HR-TEM experiments and the related analysis. V.D. and T.I. analyzed data and discussed the results. S.N.Y. drafted the manuscript with input from all authors. All the authors discussed the results and commented on the manuscript.

COMPETING INTERESTS

K.B., N.S., M.A., V.D. T.I., and S.N.Y, are inventors on a PCT application related to this work, that is currently under review with the World Intellectual Property Organization (WIPO, filing no. /PCT/GR2021/00029/2021-01881, 11 May 2021). The other authors declare that they have no competing interests.

ADDITIONAL INFORMATION

Supplementary information The online version contains supplementary material available at https://doi.org/10.1038/s41699-022-00331-7.

Correspondence and requests for materials should be addressed to Spyros N. Yannopoulos.